Numerical Modelling Of Two-Way Out-Of-Plane Bending Tests On URM Walls The Influence Of Lateral Boundary Conditions

Chang, L.; Rots, J.G.; Esposito, R.

Publication date
2020

Document Version
Accepted author manuscript

Published in
17th International Brick/Block Masonry Conference (17thIB2MaC 2020)

Citation (APA)
Chang, L., Rots, J. G., & Esposito, R. (2020). Numerical Modelling Of Two-Way Out-Of-Plane Bending Tests On URM Walls: The Influence Of Lateral Boundary Conditions. In *17th International Brick/Block Masonry Conference (17thIB2MaC 2020)* Taylor and Francis. https://www.taylorfrancis.com/books/e/9781003098508/chapters/10.1201/9781003098508-30

Numerical modelling of two-way out-of-plane bending tests on URM walls: the influence of lateral boundary conditions

L. Chang, J. G. Rots & R. Esposito
Delft University of Technology, Faculty of Civil Engineering and Geosciences, Delft, The Netherlands

ABSTRACT: Research has shown that lateral boundary conditions can have a large influence on the force capacity of two-way spanning unreinforced masonry (URM) walls subjected to out-of-plane (OOP) loading. Differently than laterally free one-way spanning walls, they show a higher force capacity, which however is underestimated by current analytical formulations. By means of nonlinear finite element analyses adopting a detailed 3D brick-to-brick model, the influence of lateral boundary conditions on two-way out-of-plane failure of a single wythe masonry wall is studied. Results indicate that the cracking pattern varies as lateral boundaries become stiffer, accordingly the force capacity increases. Numerical results are compared with analytical formulation proposed in the Australian Standard AS3700. These preliminary results will serve to evaluate how to consider the lateral boundary conditions, provided by the wall-to-wall connection, for two-way spanning walls in existing buildings.

1 INTRODUCTION

Out-of-plane (OOP) failure of two-way spanning unreinforced masonry (URM) walls can be possibly the most dangerous failure mechanism for masonry structures during strong earthquakes (Sorrentino et al., 2016). Though this type of failure is attracting more interest in academia, some crucial factors having major influence on the force capacity of walls remain to be further studied, for example, lateral boundary conditions.

Recently, researchers have put effort in evaluating the force capacity of two-way spanning walls through both experiments and analytical formulations. Nevertheless, focuses on boundary conditions are quite limited. Griffith et al. (2007) carried out tests on two-way spanning walls subjected to cyclic loads with lateral boundaries restrained by return walls. This is close to practice however the flexibility of return wall was not estimated. A similar testing campaign was conducted at Delft University of Technology (Damiola et al., 2018) in which the lateral edges of walls were constrained with steel tubes and were assumed as hinged. In fact, the lateral boundaries of walls in reality are mostly partially clamped considering they are restrained by return walls which are able to transfer part of bending moments. This situation leads to a difficulty in accurately predicting the force capacity of walls. In Eurocode 6 (EN1996-1-1, 2012) where yield line method is applied, boundary conditions of two-way spanning walls are calculated as either hinged or clamped. This obviously misevaluate the boundary conditions. Australian Standard – Masonry Structures (AS3700-2011, 2011) which is based on virtual work method quantifies lateral boundaries with coefficient R_f. The lateral boundaries are hinged with $R_f = 0$ or clamped with $R_f = 1$. Still, the code notifies that walls constrained within intermediate situations (e.g. with return walls) should be evaluated by users and an intermediate value R_f has not been recommended. Willis (2004) proposed an update for virtual work method where torsional strength of masonry was introduced to evaluate diagonal bending capacity. Griffith and Vaculik (2007) found that when R_f is assumed as 0.5 the prediction of the updated method could be the most close to testing results for two-way spanning walls with return walls. This was also confirmed by parametric study by Damiola et al. (2018). However, according to testing results by Graziotti et al. (2019), the value of masonry torsional strength can influence the accuracy of evaluation on the wall capacity. Based on aforementioned discussion, a research gap can be identified that experiments focusing on lateral boundary conditions of two-way spanning URM walls are limited and evaluation of those by analytical formulations in current codes need to be improved.

The aim of this paper is to study the influence of lateral boundary conditions on the force capacity of two-way spanning URM walls and provide basis for improving related part in current codes. With this goal, numerical simulation was firstly applied to

model two-way OOP bending test for URM wall performed at Delft University of Technology (Damiola et al., 2018). Subsequently, a parametric study was carried out considering various flexibility of lateral boundaries based on previous model. Finally, numerical results were compared with Australian Standard and revised formulations using experimentally derived torsional shear strength provided by Graziotti et al. (2019).

2 TWO-WAY OOP BENDING TESTS

The two-way OOP bending tests were carried out at Delft University of Technology (Damiola et al., 2018). Testing sample TUD_COMP-11 was selected as reference for numerical models in this study. This sample was made of calcium silicate bricks and cement based mortar. The dimension of bricks was 214 × 72 × 102 mm^3 while the thickness of mortar joint was 10 mm. The dimension of the wall was 3874 × 2765 × 102 mm^3. The test set-up of the wall is shown in Figure 1.

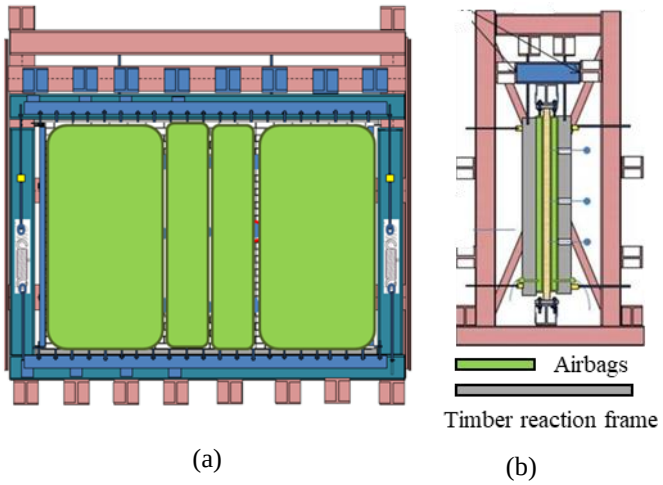

(a) (b)

Figure 1. Test set-up for wall TUD_COM-11 (Ravenshorst and Messali, 2016).

The wall was constrained on four sides. Along top and bottom boundaries, the wall was glued to strengthened steel beams (Fig. 2(a)). At the top the wall was allowed to move vertically. Along lateral sides, steel tubes were applied and wooden edges were inserted between steel tubes and the wall to prevent local damage (Fig. 2(b)).

The wall was firstly loaded with a pre-compression of 0.05 N/mm^2 at the top. Afterwards, horizontal cyclic load was uniformly applied to the wall by means of airbags placed against both front and back sides of the wall. Initially airbags on both sides were pumped to certain pressure. Then pressure of airbag on back side of the wall was kept unchanged while pressure within the airbag on the front side was varied in a cyclic manner. The cyclic load was displacement-controlled with regard to the very central point of the wall. Additional tests were carried out to determine increment caused by friction between the wall and the airbags. More details about boundary conditions and loading protocol were discussed in Ravenshorst and Messali (2016) and Damiola et al. (2018). Table 1 lists material properties from material tests using the same batch of bricks and mortar.

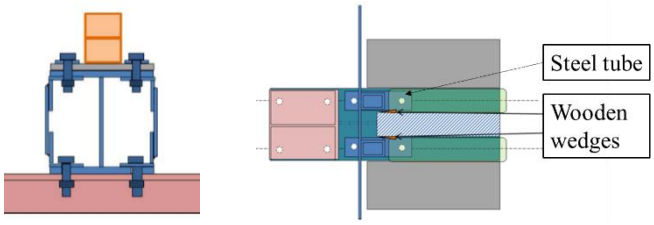

(a) (b)

Figure 2. Boundary conditions for wall TUD_COMP-11: (a) bottom boundary condition; (b) lateral boundary condition (Ravenshorst and Messali, 2016).

Table 1. Material properties from material tests.

Material properties	Symbol	Units	Average	C.o.V	Testing standard
Density of masonry	ρ	kg/m^3	1910	-	-
Elastic modulus of brick units	E_b	MPa	8990	0.36	EN 772-1
Poisson's ratio	v	-	0.16	-	EN 772-1
Flexural bond strength	f_w	MPa	0.27	0.43	EN 1052-5
Cohesion	$_c$	MPa	0.14	-	EN 1052-3
Friction angle	ϕ	rad	0.406	-	EN 1052-3
Compressive strength	f_c	MPa	5.93	0.09	EN 1052-1
Compressive fracture energy	$G_f{}^c$	N/mm	31.5	0.16	EN 1052-1

3 NUMERICAL MODELS

3.1 *Modelling technique*

Nonlinear finite element analyses were carried out by adopting a 3D brick-to-brick model including geometrical and physical nonlinearity. The simplified modelling technique proposed by Lourenco and Rots (1997) was adopted in which bricks are extended with regard to their original dimensions while mortar joints are modelled with zero-thickness interface elements. 20-node solid elements were used to model the bricks, while 8-node interface elements were adopted for the mortar joints. Symmetric model was adopted (Fig. 3). Clamped restraints were imposed at the top and bottom side of the wall, but allowing the vertical displacement of the top side of the wall. In view of the parametric study on the lateral boundary conditions, presented in Section 5, the laterally hinged connections were modelled by means of boundary interface elements with an elastic normal stiffness equal to $k_{n,lateral}$ = 0.0001 N/mm^3. Self-weight and pre-compression (0.05 N/mm2) were applied to the model.

Differently than in the experiment, a monotonic analysis was performed applying a uniform pressure on the face of the wall and adopting arc-length control. Quasi-Newton solution method was adopted. The analyses were carried out with FEA software DIANA version 10.3 (DIANA.BV., 2019).

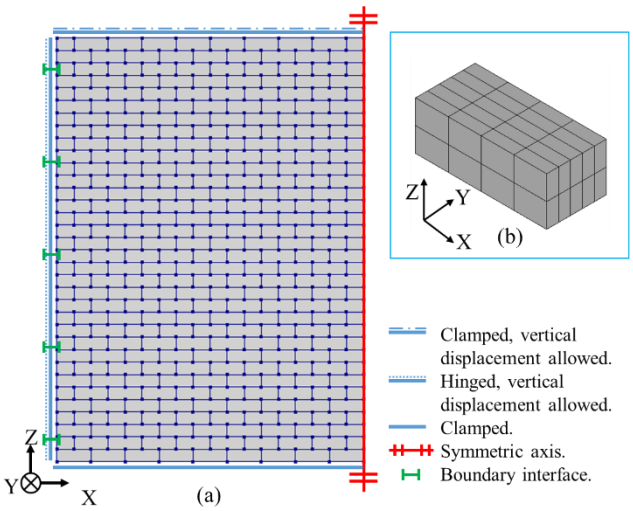

Figure 3. Numerical model of TUD_COMP-11: (a) boundary conditions; (b) meshing for a single block.

To describe the nonlinear response of the masonry, the Multi-surface Interface Model (Lourenco and Rots, 1997, Rots, 1997) was used, while bricks were modelled as linear elastic. The multi-surface plasticity model comprises a Coulomb friction model, a tension cut-off and an elliptical compression cap (Fig. 4). Softening acts in all three modes. In the elastic stage, the normal stiffness and shear stiffness of interface elements were calculated based on elastic modulus of bricks, elastic modulus of mortar, mortar joint thickness and Poisson ratio (Lourenco and Rots, 1997):

$$k_n = \frac{E_{unit}E_{joint}}{h(E_{unit}-E_{joint})} \quad (1)$$

$$k_s = \frac{G_{unit}G_{joint}}{h(G_{unit}-G_{joint})} \quad (2)$$

$$G_{unit} = \frac{E_{unit}}{2(1+\nu_{unit})} \quad (3)$$

$$G_{joint} = \frac{E_{joint}}{2(1+\nu_{joint})} \quad (4)$$

where E_{unit}, G_{unit} and ν_{unit} the elastic modulus, shear modulus and Poisson's ratio of brick unit respectively; E_{joint}, G_{joint} and ν_{joint} elastic modulus, shear modulus and Poisson's ratio of mortar joint respectively; k_n and k_s normal stiffness and shear stiffness of interface elements respectively; h the thickness of mortar joints.

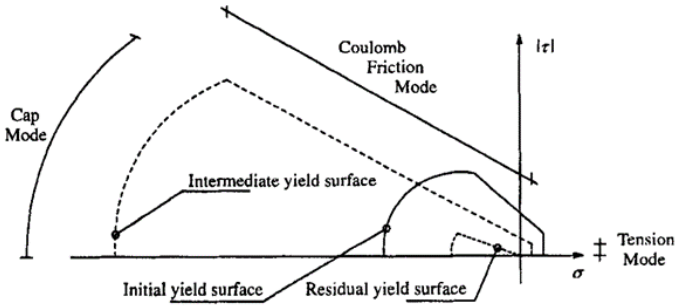

Figure 4. Multi-surface interface model for interface elements (Lourenco and Rots, 1997).

3.2 *Calibration of input parameters*

Material properties used as input for numerical models were directly retrieved from or calibrated based on small-scale material tests performed in the same testing campaign (Esposito et al., 2016, Jafari et al., 2019).

Calcium silicate brick units are modelled as linear elastic solid elements, elastic modulus and Poisson's ratio were retrieved from flexural strength test of masonry unit. Since the elastic modulus of mortar joints was not experimentally determined, the normal stiffness of bed joint, $k_{n,bed}$, was calibrated to match the initial stiffness of numerical model with that of experiment. The calibrated value of $k_{n,bed}$ was then used to calculate the elastic modulus of the mortar joint E_{joint} through equation (1). According to construction practice, mortar in bed joints can be generally considered stronger than that one in head joints. In this sense, the normal stiffness of head joints $k_{n,head}$ was defined two times smaller than the normal stiffness of bed joints $k_{n,bed}$. The shear stiffness of bed joints, $k_{s,bed}$, and shear stiffness of head joints, $k_{s,head}$, were calculated through equation (2) - (4).

With regard to material properties related to the nonlinear behaviour, tensile strength f_t and Mode-I fracture energy G_f^I were calibrated according to bond wrench tests and OOP masonry wallet tests respectively; cohesion c, friction angle ϕ and Mode-II fracture energy G_f^{II} were retrieved or calibrated from masonry shear triplet tests; compressive strength f_c and compressive fracture energy G_{fc} were retrieved from masonry compression tests. Note that the same reduction factor α was also applied between $f_{t,bed}$ and $f_{t,head}$. Since shapes of softening and compression cap of bed joints and head joints are assumed to be the same, fracture energy of head joints is approximately ¼ of that of bed joints. The adopted input parameters are given in Table 2 and Table 3.

Table 2. Input parameters for bricks.

Input parameters	Symbol	Units	Value
Young's modulus	E_b	N/mm^2	8990
Poisson's ratio	ν_b	-	0.16
Mass density	ρ	kg/m^3	1910

Table 3. Input parameters for interface elements.

Input parameters	Symbol	Units	Bed joints	Head joints
Normal stiffness	k_n	N/mm^3	28.9	14.22
Shear stiffness	k_s	N/mm^3	12.46	6.13
Tensile strength (2/3 of f_w)	f_t	MPa	0.18	0.09
Mode-I fracture energy	$G_f{}^I$	N/mm	0.016	0.004
Cohesion	f_{v0}	MPa	0.14	0.07
Friction angle	ϕ	rad	0.406	0.406
Residual friction angle	ϕ_{res}	rad	0.406	0.406
Mode-II fracture energy	$G_f{}^{II}$	N/mm	0.01	0.0025
Compressive strength	f_c	MPa	5.93	2.97
Compressive fracture energy	$G_f{}^c$	N/mm	31.5	7.88

4 NUMERICAL RESULTS

In this section, numerical results are presented and compared with experimental results in terms of lateral force vs. mid-span displacement curves (Fig. 5) and crack pattern (Fig. 6). According to previous study, the revised experimental envelope curve was considered for comparison to exclude the fictitious force increment caused by the friction between the wall and airbags (Damiola et al., 2018). The numerical results show a linear behaviour up to a displacement of approximately 9 mm (point A in Fig. 5(b)) followed by a sharp reduction in capacity after the peak (points B and C) and a subsequent hardening behaviour until a displacement of approximately 30 mm (point D). After this point, no convergent results could be achieved.

Compared with experimental curve, the initial stiffness and peak force of numerical model matched well with those of testing results (13.96 kN/mm vs. 12.00 kN/mm and 29.38 kN vs. 28.9 kN). This suggests that calibration of material properties is appropriate and values retrieved directly from material tests are suitable for modelling large-scale walls.

The lateral force vs. mid-span displacement curve was in general in agreement with testing results, except that the peak force in numerical model appeared much earlier than in tests. Besides, a sharp drop in force after peak force was not experimentally observed in testing curve. Additional parametric study with respect to f_t, $G_f{}^I$, c and $G_f{}^{II}$ has shown that as these values varied, there were no obvious changes in this drop of force. This difference can be caused by that in test the lateral load was cyclic while it was monotonic in numerical model. Since the largest displacement for each loading cycle was gradually increased and there was unloading during each cycle, both horizontal cracks and diagonal cracks could develop more evenly. Besides, moment resistance capacity along developing cracks could be redistributed over time. This can lead to a continuously increase of force capacity. In contrast, in a monotonic loading test, there was a sequence for cracking at different locations, increase of force capacity is possible after a period of decrease. A similar trend with a sharp drop in force after the attainment of the maximum lateral force was experimentally observed by Griffith et al. (2007) during monotonic tests on full-scale walls.

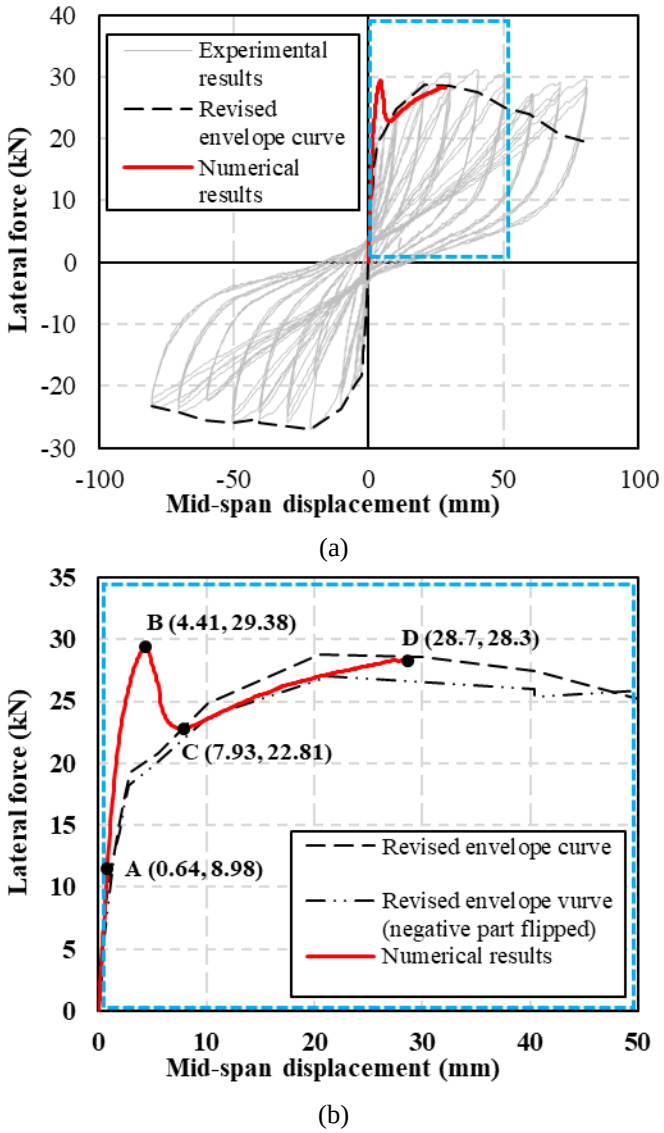

Figure 5. Lateral force vs. mid-span displacement curves of experimental and numerical results: (a) full graph; (b) Close-up graph.

The evolution of cracking is shown in Figure 6 where crack opening of interface elements is shown. Here four sub-figures corresponding to the four critical points A-D marked in Figure 5(b) are considered. At Point A, two long horizontal cracks firstly develop along bed joints adjacent to top and bottom sides of the wall. This marks the onset of nonlinear behaviour. When horizontal cracks are fully developed along the length of the wall (Point B), the wall reached its peak force (29.38 kN). As displacement increases, the force capacity of the wall starts to decrease till diagonal cracks fully develops (Point C, 22.81 kN). Then the force capacity starts to increase again which can be due to an arching effect. The final crack pattern at point D is composed of horizontal cracks at the top,

bottom and central mortar bed joint, diagonal cracks starting few courses away from the corner of the wall, and corner cracks; this crack pattern is in agreement with experimental observations (Fig. 6(e, f)).

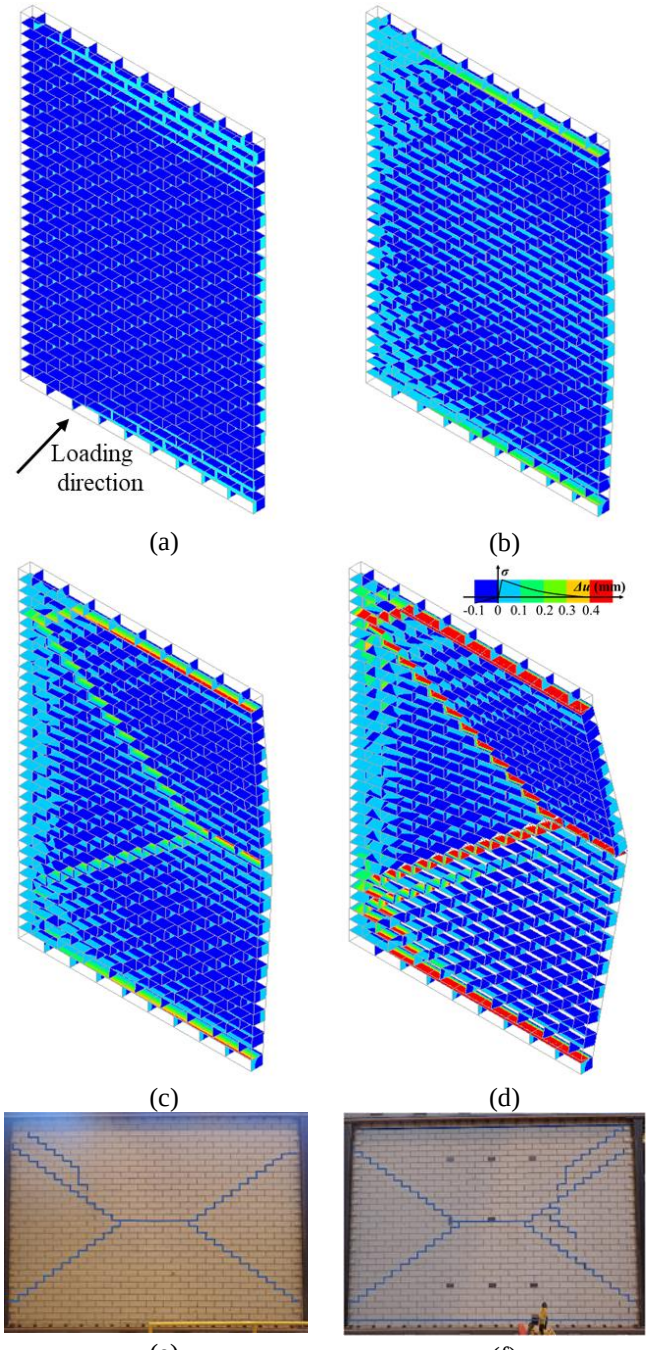

Figure 6. (a) - (d) Cracking pattern at relevant load levels (Figure 5) obtained by numerical analysis (deformation scale factor: 10; symmetric axis at right side); (e) - (f) experimental cracking pattern at back and front side of the wall.

To evaluate the influence of different local failure mechanisms, a detailed analysis was performed by analysing the local failure mechanisms in three main cracks (Fig. 7). The horizontal crack at the top of the wall (front side), the diagonal crack (back side) and the crack at the corner (front side) were considered. Absolute values at integration points are presented. For the horizontal crack, crack opening (normal relative displacement of the interface) and limited in-plane shear and out-of-plane sliding are observed, suggesting as expected, that tensile failure is the main failure mechanism for horizontal cracks (Fig. 7(a)). For the diagonal crack (Fig. 7(b)), both cracking opening and in-plane shear sliding play an important role. At corner crack (Fig. 7(c)), all three failure mechanisms are observed, but their deformation are lower with respect to the other two cracks analysed.

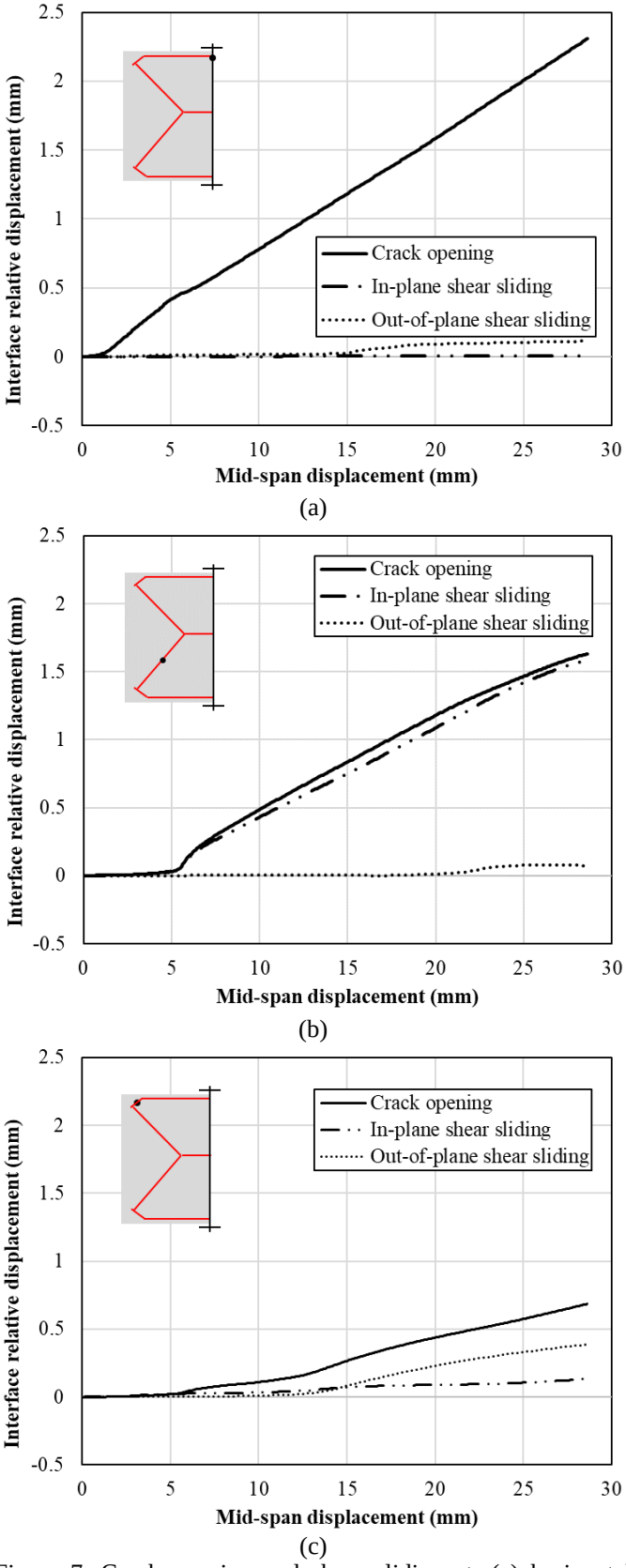

Figure 7. Crack opening and shear sliding at: (a) horizontal crack, (b) diagonal crack and (c) corner crack.

5 PARAMETRIC STUDY ON THE STIFFNESS OF LATERAL BOUNDARY CONDITIONS

The main aim of this paper is to study the influence of lateral boundary conditions on mechanical behaviour of two-way spanning URM walls subjected to OOP loading. For this purpose, the normal stiffness of the lateral boundary interface element, $k_{n,lateral}$, was varied to model lateral boundaries with different rotational stiffness. As $k_{n,lateral}$ increases from 0.0001 N/mm^3 (hinged case already discussed in Section 4) to 10000 N/mm^3, the lateral boundary can be deemed as changing from hinged (free rotation along Z axis) to clamped (rotation constrained along Z axis). Five cases are considered, among which three different cases to represent the partially clamped case ($k_{n,lateral}$ = 1 N/mm^3; $k_{n,lateral}$ = 5 N/mm^3; $k_{n,lateral}$ = 10 N/mm^3). Numerical results are shown in Figure 8, together with previously discussed experimental results for the hinged case. Please note that in this section the partially clamped case 2 is further selected for comparison with hinged and clamped cases.

By increasing the stiffness of rotational restraints at the lateral boundaries (from hinged to clamped case) both initial stiffness and force capacity of two-way OOP bending URM wall increased as expected (Table 4 and Figure 8). Furthermore, the sharp drop in force observed by for the hinged case at the onset of diagonal cracking is gradually reduced for partially clamped cases and it is not observed for the clamped case.

By increasing the stiffness of rotational restraints at the lateral boundaries, besides the formation of horizontal, diagonal and corner cracks as observed for the hinged case, vertical cracks at the lateral sides become predominant. To compare this difference, the crack evolution for the hinged case, the partially clamped case 2, and the clamped case can be summarised as follows:

- Hinged case : horizontal cracks → corner cracks (not obvious) → diagonal cracks
- Partially clamped case 2: horizontal cracks → corner cracks → diagonal cracks → vertical cracks
- Clamped case: horizontal cracks → vertical cracks → corner cracks → diagonal cracks

The presence of vertical cracks for the partially clamped and for the clamped case can be reasonable ascribed to the increase in bending moments. Larger bending moments lead to larger tensile stresses along joints at lateral boundaries resulting in vertical cracks. This reasoning can also explain the different cracking sequences between the partially clamped case 2 and the clamped case. Since the rotational stiffness of lateral boundaries for the clamped case is larger than that one for the partially clamped case 2, larger lateral bending moments can lead to an earlier development of vertical cracks.

It is worthy to note that in the paper by Griffith et al. (2007) a two-way spanning URM wall sample laterally restrained by return walls with similar pre-test set-up as wall TUD_COMP-11 showed a same cracking process as for partially clamped case 2 in this paper. This suggests that a two-way spanning URM wall in reality is neither clamped nor hinged along lateral boundaries but at a partially clamped state.

Table 4. Comparison in terms of initial stiffness and peak force.

Cases	$K_{n,lateral}$ (N/mm^3)	Initial stiffness (kN/mm)	Peak force (kN)
Hinged	0.0001	13.96	29.38
Partially clamped 1	1	14.25	41.88
Partially clamped 2	5	15.09	54.09
Partially clamped 3	10	15.72	57.71
Clamped	10000	17.95	64.61
Experiment	-	12.00	28.90

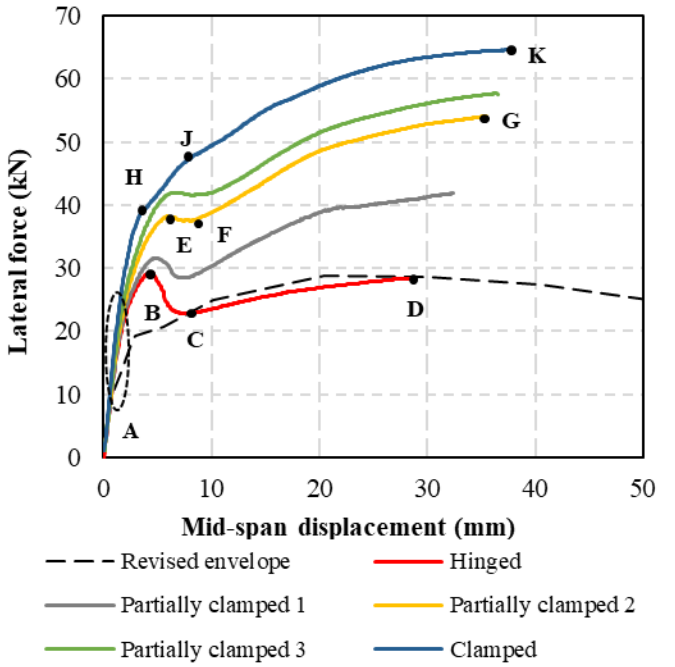

Figure 8. Lateral force vs. mid-span displacement curves of various lateral boundary conditions.

Five locations, I-V in Figure 9 are selected to check the local failure mechanisms for the three cases. Figure 9(a) shows that as rotational stiffness of lateral boundaries increases, crack opening decreases at location II while it increase at location IV and V. In Figure 9(b, c) it is shown that as lateral boundaries become stiffer, both in-plane and out-of-plane shear sliding decrease at location II. At location III, in-plane shear sliding increases while out-of-plane shear sliding decrease as lateral boundaries become stiffer. At location IV and V, both in-plane and out-of-plane shear increase as the rotational stiffness of lateral boundaries increase. This is because stiffer lateral boundaries on one hand constrain developing of diagonal cracks, on the other hand they lead to larger bending moment along vertical edges that causes larger crack opening and shear sliding.

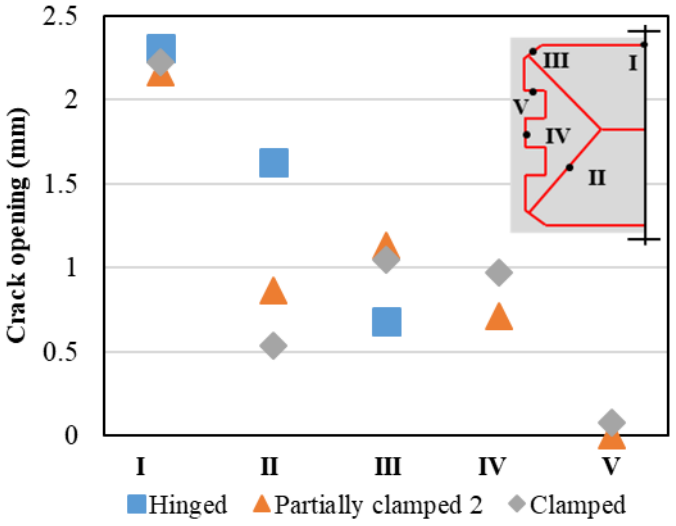

(a)

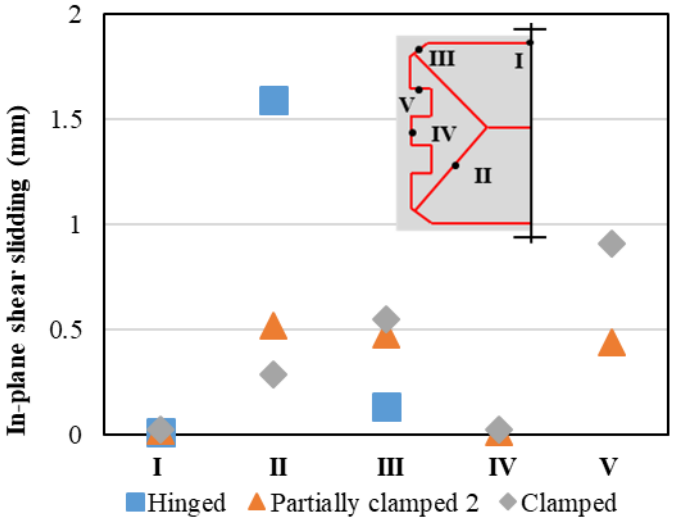

(b)

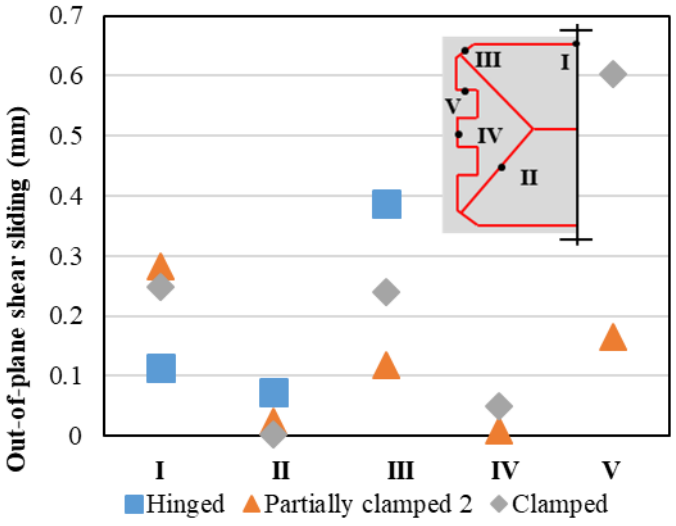

(c)

Figure 9. Comparison of cracking mechanisms: (a) crack opening; (b) in-plane shear sliding; (c) out-of-plane shear sliding.

6 COMPARISON WITH ANALYTICAL FORMULATIONS

Australian standard AS3700 (AS3700-2011, 2011) currently provides the most advanced analytical formulations on predicting the force capacity of two-way spanning URM walls. This is because it applies virtual word method and comprehensively evaluates various crucial factors such as boundary conditions, aspect ratio and openings that have major influence on wall behaviour. However, in some cases, it still largely underestimates the wall capacity. According to Damiola et al. (2018), AS3700 underestimated the capacity of single wythe clay wall up to -56% when lateral boundaries were considered as hinged. The large error was caused by an incorrect prediction of cracking pattern by AS3700, which considered the formation of a vertical crack at the centre of the wall instead of the experimentally observed horizontal crack. This raised the doubt on the accuracy of the analytical formulation, in particularly questioning the definition of the restrain coefficient R_f and the definition of the torsional strength.

To further study the influence of lateral boundary conditions, force capacity of the wall was calculated based on Australian Standard AS 3700 (AS3700-2011, 2011) and revised formulas proposed by Willis (2004). The torsional shear strength in later formulas were replaced with experimental results provided by Graziotti et al. (2019). From Figure 10 it can be seen that if lateral boundaries are considered as hinged (R_f = 0 in AS 3700) or clamped (R_f = 1), AS3700 either underestimates (-22%) or overestimates (+48%) the wall capacity. If lateral boundaries are considered as partially clamped (R_f = 0.5), the standard provides a more accurate prediction with an error of +13%. By now an intermediate value for R_f has not been proposed by AS3700 (AS3700-2011, 2011). Griffith and Vaculik (2007) and (Graziotti et al., 2019) suggested that R_f can be 0.5 but this requires further verification.

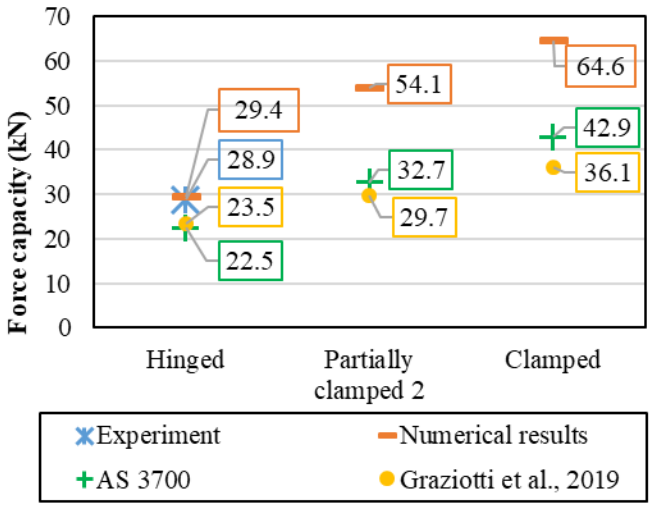

Figure 10. Comparison of force capacity with analytical formulations.

7 CONCLUSIONS

This paper focuses on the influence of lateral boundary conditions on response of two-way spanning URM walls subjected to out-of-plane (OOP) loading.

For this purpose, nonlinear finite element analyses adopting a detailed 3D brick-to-brick model were carried out to evaluate the influence of lateral boundary conditions on the force capacity of two-way spanning URM walls. A parametric study was conducted to evaluate the influence of lateral boundary conditions and results were compared with analytical formulations proposed by Australian Standard AS3700 and Willis (2004) respectively. Here torsional stiffness in formulations by Willis (2004) were replaced with experimental values by Graziotti et al. (2019). The following observations and conclusions can be drawn:

- Using material properties directly retrieved from small-scale material tests combined with minor calibrations, a good agreement between numerical and experimental results in terms of initial stiffness, force capacity and cracking pattern was obtained. This suggests that material properties measured in small-scale material tests are suitable for modelling large-scale two-way OOP spanning URM wall components.
- Differently than observed in the experiment, the numerical results for the case with hinged lateral boundary conditions shows an initial drop in force before the formation of the diagonal cracks. This can be caused by different loading protocol between numerical model and experiment. In experiment the loading was cyclic while in numerical model it was monotonic.
- The parametric study shows that as the rotational stiffness of lateral boundaries increased, both initial stiffness and force capacity of two-way spanning walls increased. Also, the evolution of cracks and the final cracking pattern varied as lateral boundary conditions changed. Vertical cracks were not observed for the hinged case ($k_{n,lateral}$ = 0.0001 N/mm^3), while they were observed both for the partially clamped case 2 ($k_{n,lateral}$ = 5 N/mm^3) and the clamped case ($k_{n,lateral}$ = 10000 N/mm^3). Furthermore, as the lateral boundaries become rotationally stiffer, vertical cracks occurred for a lower mid-span displacement. This causes an internal redistribution of the moments leading to an increase initial stiffness and force capacity of the wall.
- A quantitative analysis of local failure mechanisms occurring in the main cracks was carried out and comparison between the three cases was made. A general tendency is that as rotational stiffness of lateral boundaries increases, crack opening, in-plane shear sliding and out-of-sliding increase at vertical cracks along lateral boundaries accordingly while they decrease at diagonal cracks.
- Either considering lateral boundaries as hinged or clamped when applying AS 3700 can be inaccurate. In contrast, assuming lateral boundary as partially clamped provides the most accurate prediction. A determined R_f value needs to be quantified for walls in practice. Meanwhile, the accuracy in terms of predicting cracking pattern by AS3700 should also be improved.

Based on aforementioned conclusions, it implies that assuming lateral boundaries of two-way spanning URM walls as either hinged or clamed is inaccurate when applying analytical formulations. More research is suggested to quantitatively evaluate the stiffness of lateral boundary conditions and further improve the accuracy of analytical formulations.

REFERENCE

AS3700-2011 (2011) Australian standard of masonry structures. *AS 3700*.

DAMIOLA, M., ESPOSITO, R., MESSALI, F. & ROTS, J. G. (2018) Quasi-static cyclic two-way out-of-plane bending tests and analytical models comparison for URM walls. *10th International Masonry Conference.* Milan, Italy.

DIANA.BV. (2019) *DIANA user's manual - Release 10.3*, Delft, The Netherlands.

EN1996-1-1 (2012) Eurocode 6: Design of masonry structures—Part 1-1: General rules for reinforced and unreinforced masonry structures. *Comité Européen de Normalisation: Brussels, Belgium.*

ESPOSITO, R., MESSALI, F. & ROTS, J. G. (2016) Tests for the characterization of replicated masonry and wall ties. Delft, The Netherlands.

GRAZIOTTI, F., TOMASSETTI, U., SHARMA, S., GROTTOLI, L. & MAGENES, G. (2019) Experimental response of URM single leaf and cavity walls in out-of-plane two-way bending generated by seismic excitation. *Construction and Building Materials,* 195**,** 650-670.

GRIFFITH, M. C. & VACULIK, J. (2007) Out-of-plane flexural strength of unreinforced clay brick masonry walls. *TMS Journal,* 25**,** 53-68.

GRIFFITH, M. C., VACULIK, J., LAM, N. T. K., WILSON, J. & LUMANTARNA, E. (2007) Cyclic testing of unreinforced masonry walls in two-way bending. *Earthquake Engineering & Structural Dynamics,* 36**,** 801-821.

JAFARI, S., ESPOSITO, R. & ROTS, J. G. (2019) From Brick to Element: Investigating the Mechanical Properties of Calcium Silicate Masonry. Cham, Springer International Publishing.

LOURENCO, P. B. & ROTS, J. G. (1997) Multisurface interface model for the analysis of masonry structures. *Journal of Structural Engineering-Asce,* 123**,** 660-668.

RAVENSHORST, G. J. P. & MESSALI, F. (2016) Out-of-plane tests on replicated masonry walls. Delft University of Technology.

ROTS, J. G. (1997) *Structural Masonry,* Netherlands, A.A.Balkema.

SORRENTINO, L., D'AYALA, D., DE FELICE, G., GRIFFITH, M. C., LAGOMARSINO, S. & MAGENES, G. (2016) Review of Out-of-Plane Seismic Assessment Techniques Applied To Existing Masonry Buildings. *International Journal of Architectural Heritage***,** 1-20.

WILLIS, C. (2004) Design of Unreinforced Masonry Walls for Out-of-plane Loading. Adelaide, Australia, The University of Adelaide.